APPLIED SCIENCES AND ENGINEERING

IRONSperm: Sperm-templated soft magnetic microrobots

Veronika Magdanz[1]*, Islam S. M. Khalil[2]*, Juliane Simmchen[3], Guilherme P. Furtado[2],
Sumit Mohanty[2], Johannes Gebauer[1], Haifeng Xu[4], Anke Klingner[5], Azaam Aziz[4],
Mariana Medina-Sánchez[4], Oliver G. Schmidt[4,6,7], Sarthak Misra[2,8]

We develop biohybrid magnetic microrobots by electrostatic self-assembly of nonmotile sperm cells and magnetic nanoparticles. Incorporating a biological entity into microrobots entails many functional advantages beyond shape templating, such as the facile uptake of chemotherapeutic agents to achieve targeted drug delivery. We present a single-step electrostatic self-assembly technique to fabricate IRONSperms, soft magnetic microswimmers that emulate the motion of motile sperm cells. Our experiments and theoretical predictions show that the swimming speed of IRONSperms exceeds 0.2 body length/s (6.8 ± 4.1 μm/s) at an actuation frequency of 8 Hz and precision angle of 45°. We demonstrate that the nanoparticle coating increases the acoustic impedance of the sperm cells and enables localization of clusters of IRONSperm using ultrasound feedback. We also confirm the biocompatibility and drug loading ability of these microrobots, and their promise as biocompatible, controllable, and detectable biohybrid tools for in vivo targeted therapy.

INTRODUCTION

Minimally invasive surgery and targeted therapy by the help of microrobots are innovative techniques to simultaneously reduce the level of intervention, concentrate a drug in certain locations, and thereby mitigate the risks of negative side effects. These untethered microrobots can physically access small spaces in a noninvasive manner. This feature is expected to help clinicians cope with diseases that require access to difficult-to-reach regions in the human body (1–3). The controlled delivery of these devices in vivo would require them to overcome the following hurdles: first, to swim controllably under the influence of external stimuli [magnetic (4–7), chemical (8), ultrasound (9), magnetoacoustic (10), electric (11), or light (12)]; second, to provide a relatively high contrast-to-noise ratio during localization via medical imaging systems (13–15); third, to carry a cargo toward a desired location (6, 16); and last, to consist of elements with a certain degree of biocompatibility (17). Biological and biohybrid microrobots combine these requirements owing to their high motility, sensing ability, adaptation to physiological conditions, and magnetic response (18). On the one hand, the biohybrid approach capitalizes on the propulsive force of motile sperm cells, algae, bacteria, or the contractile force of cardiac muscle cells as onboard actuators (19–25). For instance, a layer of contractile cardiomyocytes was used as the driving mechanism of a synthetic flagellum to produce propulsive force in low Reynolds numbers (19). Bacterial biohybrid microrobots are driven by flagella and exhibit pH-tactic, aerotactic, and chemotactic behavior (26–28). For instance, Felfoul et al. (28)

have translated the bacteria *Magnetococcus marinus* strain MC-1 into in vivo targeted therapy and transported drug-loaded nanoliposomes into hypoxic regions of the tumor. In the biohybrid approach of using sperm cells, the motile cells are captured in microtubes where the cell imparts a propulsive force to the fluid, while the microtube provides a magnetic dipole for directional control (20). Sperm micromotors have also been shown to deliver anticancer drugs locally to cancer spheroids (29).

On the other hand, another proposed method to develop biohybrid microrobots uses spiral microstructures from plants and other organisms as biological templates (30, 31). Gao et al. (30) have developed helical microswimmers from spiral water-conducting vessels of different vascular plants and demonstrated locomotion in human serum. Kamata et al. (31) have also fabricated microelectromagnetic coils by a biotemplating process in which a metal coating was deposited onto the surface of *Spirulina* microalgae. Further, biohybrid magnetic microrobots have been fabricated from microalgae by Yan et al. (14) via a dip-coating process in magnetite suspensions, and in vivo fluorescence-based localization was achieved inside rodent stomachs. Porous microneedles from plants or pollen-derived microstructures demonstrated cellular drilling and drug administration under the action of external magnetic fields (32, 33). These fabrication methods enable fabrication of arbitrarily shaped microrobots based on the template obtained from nature, mostly in the shape of a helix or filament.

Most of these biotemplating approaches produced rigid microrobots, but specific additional beneficial features lie in the creation of soft and flexible microrobots. It is important to note that the ability to change shape allows the movement through tight spaces or winding channels (34). Further, the ability to interact with soft tissue and cells without mechanical damage is crucial for biomedical applications (35). Previously, an artificial robotic sperm was developed by electrospinning to create a flexible polystyrene tail with a magnetic head (36). This millimeter-sized robotic sperm was actuated with oscillating magnetic fields and demonstrated forward motion of up to 0.9 body length/s. However, this flexible robotic sperm is relatively large, and its components are not biocompatible. In

[1]Applied Zoology, Faculty of Biology, Technical University of Dresden, Dresden, Germany. [2]Department of Biomechanical Engineering, University of Twente, Enschede, Netherlands. [3]Physical Chemistry, Technical University of Dresden, Dresden, Germany. [4]Institute for Integrative Nanosciences, Leibniz Institute for Solid State and Materials Research, Dresden, Germany. [5]Department of Physics, German University in Cairo, New Cairo City, Egypt. [6]Center for Materials, Architectures and Integration of Nanomembranes, Chemnitz University of Technology, Chemnitz, Germany. [7]School of Science, Technical University of Dresden, Dresden, Germany. [8]Department of Biomedical Engineering, University of Groningen and University Medical Center Groningen, Groningen, Netherlands.
*Corresponding author. Email: veronika.magdanz@tu-dresden.de (V.M.); i.s.m.khalil@utwente.nl (I.S.M.K.)

our previous work, we presented the initial approach of attaching 1-μm large iron oxide particles to the surface of bovine spermatozoa based on electrostatic-based self-assembly. The magnetic sperm cells were actuated using uniform in-plane magnetic fields along the direction of motion with a sinusoidally varying orthogonal component, which resulted in relatively low velocities owing to the limited flexibility of the cells (37). The cells are fully covered by 1-μm iron oxide particles, resulting in a relatively small bending amplitude along the flagellum. The key to maintaining the intrinsic flexibility of the sperm cell is to use nanometer-sized particles and not a full coverage of particles onto the sperm but rather create different magnetic elements along a few locations along the sperm cell. It was reported recently that differently charged particles bind to different areas of sperm (38). In the current approach, we use this unique property and use smaller, nanometer-sized elongated particles that attach to some regions of the bovine sperm on the basis of its charge distribution.

Here, we present a sperm-templated microrobot created by a unique electrostatic-based self-assembly fabrication approach (39, 40) and described by a regularized Stokeslets-based hydrodynamic model. The fabrication approach relies on the opposite surface charges of bovine sperm cells and maghemite nanoparticles to develop microrobots via electrostatic interaction. Figure 1A displays a scanning electron micrograph of an IRONSperm. The attachment of the elongated 100-nm iron oxide particles to the head (Fig. 1B), midpiece (Fig. 1C), principal piece (Fig. 1D), and distal end (Fig. 1E) of a bovine sperm cell are shown in electron micrographs. The microrobot consists of a nonmotile bovine sperm cell coated with nanoparticles. The self-assembly process reaches an equilibrium, in which the charges between the nanoparticles and sperm membrane are balanced out. Spermatozoa do not have a uniform charge distribution (38); thus, we obtain different configurations of IRONSperms (see Fig. 2A). All IRONSperms are characterized by regions with nanoparticle coverage and uncoated regions, which ensure flexibility while providing magnetic moment for magnetic actuation and controlled flagellar propulsion. Helical flagellar propulsion in low Reynolds numbers is achieved under the influence of homogeneous magnetic fields with a periodically varying component. The nanoparticle coating improves the echogenicity of the organic body and enables localization by ultrasound images, while the organic body is loaded with a drug and controllably steered along reference trajectories using controlled magnetic fields.

RESULTS

Fabrication and characterization of IRONSperms

IRONSperms are fabricated using a suspension of rice grain–shaped maghemite nanoparticles with a 100-nm diameter and bovine sperm cells (~60 μm long). The particles in the suspension are influenced by electrostatic forces (van der Waals and Coulomb forces). The van der Waals attraction is limited and decays asymptotically as r^{-7}, where r is the distance between adjacent particles, and results in aggregation when particles collide. The formed aggregates and sperm cells are oppositely charged, thereby inducing long-range Coulomb attractive forces that decay as r_i^{-2}, where r_i is the distance between the ith aggregate and the nearest point along the sperm cell (Fig. 1F). The energy needed to bring the ith aggregate to this point must be smaller than the thermal energy (41)

$$\frac{1}{4\pi\epsilon_0}\frac{q_{ni}q_s(s)}{r_i} < 3k_B T^* \tag{1}$$

where q_{ni} is the charge of the ith aggregate of nanoparticles and $q_s(s)$ is the charge along the sperm body as a function of the arc length s. Further, ϵ_0 is the permittivity, k_B is the Boltzmann factor, and T^* is the characteristic temperature. Figure 1F shows two representative simulation results based on the electric charge balance (Eq. 1) between the sperm cell and randomly arranged nanoparticles. These particles display an average surface zeta potential of 12.9 mV in water, while sperm cells display an overall net negative surface potential (38) with nonuniform distribution of charges, also allowing areas with neutral or positive charges. The net charge of the sperm cell and the nearby aggregates determine the amount of particles that coat the sperm cell. The resulting IRONSperms are shown exemplarily in Fig. 1A in electron micrographs and in Fig. 2A in optical microscopic images. We observe a nonuniform distribution of nanoparticles along the head, midpiece, principal piece, and distal end, as displayed exemplarily by cases in Figs. 1 (B to D) and 2A. The net charge and the spatial distribution along the sperm cell are important factors in the determination of the magnetization profile and flexibility of IRONSperm. The amount of particles per cell is indicative of the magnetic response to the external magnetic field, so the magnetization is preferably high to enable actuation in the milliTesla range (2 mT) while maintaining the flexibility of the flagellum to enable flagellar wave propagation. Figure 2A shows the nonuniform coating of nanoparticles along the cell that results in distributed actuation under the influence of an external magnetic field. The particle distribution is also highly dependent on the surface charge of the sperm cells. The magnetization along the sperm cell is approximated by four magnetic dipole moments according to the four morphological distinct segments of spermatozoa $\mathbf{m}_h$ (head), $\mathbf{m}_m$ (midpiece), $\mathbf{m}_p$ (principal piece), and $\mathbf{m}_d$ (distal end), as shown in Fig. 1 (B to E).

The distributed actuation of IRONSperm is represented by approximating the magnetic dipole moment of each segment along the sperm cell. These magnetic dipole moments generate magnetic torque ($\mathbf{m}_i \times \mathbf{B}$) to counterbalance the drag torque in the medium, where $\mathbf{B}$ is the external magnetic field and i = h, m, p, d, indicating the head, midpiece, principal piece, and distal end, respectively. The governing equation of IRONSperm balances all forces normal to the body as follows (42)

$$\kappa_i\frac{\partial^4\varphi_i}{\partial s^4}(s,t) + c_{ni}\frac{\partial\varphi_i}{\partial t}(s,t) = 0 \text{ for } i = \text{h, m, p, d} \tag{2}$$

where κ_i is the bending stiffness of the ith segment along IRONSperm and $\varphi_i(s, t)$ is its tangent angle. The tangent angle is enclosed between the long axis ($\mathbf{e}_1(t)$) of the sperm and the local tangent at s. Further, c_{ni} is the normal drag coefficient of the ith segment. The force $\kappa_i\frac{\partial^4\varphi}{\partial s^4}$ tends to restore the flagellum to its original natural shape, and $c_{ni}\frac{\partial\varphi}{\partial t}$ is the viscous drag force exerted by the fluid. IRONSperms are driven by a bending moment applied by the external magnetic field at the location of the nanoparticle aggregates (Fig. 2A). These bending moments induce a traveling wave that propagates from the head to the distal end, producing a net thrust force that propels IRONSperm forward, as shown in Fig. 2B. Therefore, flexibility of the flagellum is required to achieve wave propagation and is tested
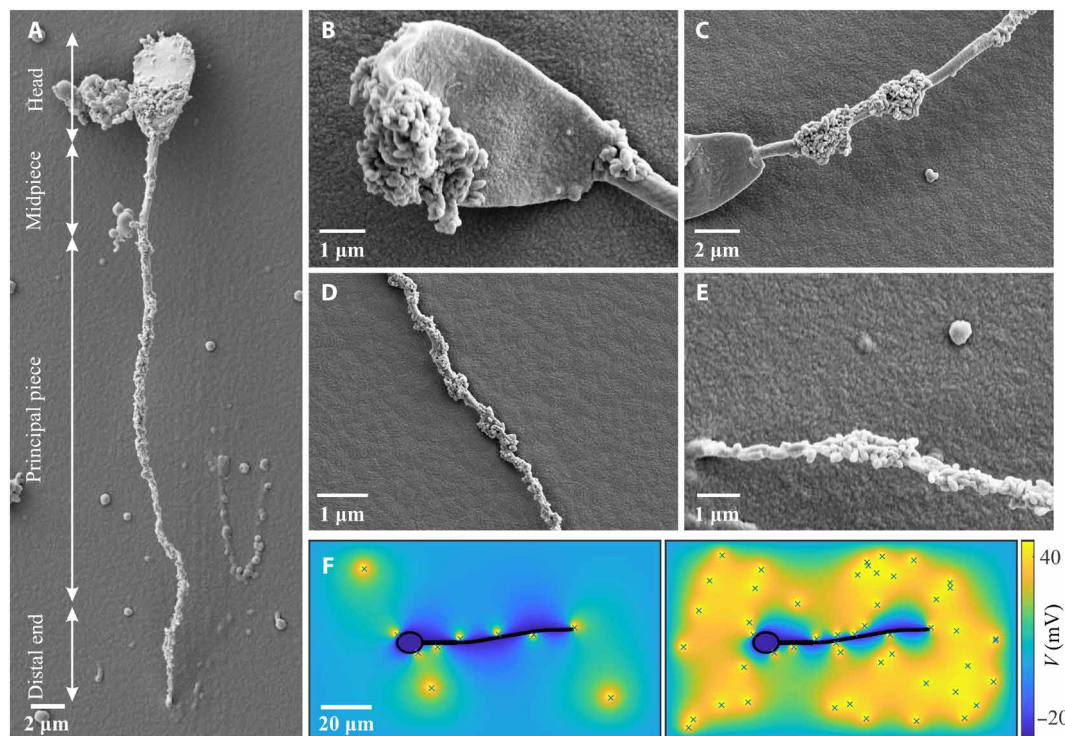
Fig. 1. Magnetite nanoparticles are attached to the head, midpiece, principal piece, and distal end of the sperm cells. (**A**) The cryo–scanning electron micrograph shows a bovine sperm cell covered with 100-nm iron oxide particles. (**B**) Sperm head, (**C**) sperm midpiece, (**D**) principal piece, and (**E**) distal end of the sperm cell with attached nanoparticles. (**F**) The density of the nanoparticles coating is based on the charge equilibrium between the sperm cell and the nanoparticles. Sperm cells and particles display negative and positive zeta potential (*V*), respectively (*1*). Nanoparticles (10 and 48 particles) are randomly distributed, and the electric potential is calculated around a sperm cell to indicate the attachment.

by allowing the sample to reside on a surface (Fig. 2C). Once adhered to the surface, a magnetic torque is exerted to observe the flexibility of IRONSperm. Figure 2C shows that the flagellum deforms with the position of the distal end fixed (see also movie S2). The blue dots indicate the trajectory of the head and represent an ellipse with minor and major diameters of 50 and 82 μm, respectively. Therefore, the flagellum of IRONSperm maintains its flexibility after the electrostatic-based self-assembly.

Although Fig. 2C indicates relatively large deformation of IRONSperm when its distal end is fixed, applying rotating magnetic field is not likely to yield the same deformation during propulsion. One valid argument that then arises is whether the motion demonstrated in Fig. 2B is due to (i) rigid body rotation of IRONSperm under the action of the rotating magnetic field or (ii) helical traveling waves along a flexible flagellum under the influence of same actuating field. In swimming motion using wave propagation along a flexible filament, the amplitude of the wave pattern is proportional to the characteristic penetration length (*43*), $\ell_w = (\kappa/\omega c_n)^{1/4}$, where ω is the angular velocity of the filament. This length depends only on the bending stiffness of the flagellum, the frequency of oscillation, and the viscosity of the medium. Variation of these parameters only affects the wave pattern in the case of propulsion with traveling waves (*44*). Therefore, we apply rotating magnetic fields at a frequency range of $3 \leq f \leq 11$ Hz. The time-dependent deformation and tangent angle of the flagellum are measured for successive intervals of motion. At each frequency, the maximum amplitude of the overall wave pattern is measured as the vertical distance between the envelopes

of motion, indicated by the dashed curves in the left column of graphs in Fig. 3. At $f = 3$ Hz, the maximum amplitude is measured as 37 μm (Fig. 3A). The amplitude decreases to approximately 30 μm at actuation frequencies of 5 and 7 Hz (Fig. 3, C and E). As the frequency increases, we observe that the overall wave pattern scales down and decreases to 23 (Fig. 3G) and 18 μm (Fig. 3I) at 9 and 11 Hz, respectively. Therefore, we attribute the propulsion of IRONSperm to the traveling wave along its flexible flagellum. Figure 3 (B, D, F, H, and J) also shows the calculated tangent angle along the flagellum based on the measured wave patterns for an actuation frequency range of $3 \leq f \leq 11$ Hz.

We measure the area covered by rice grain–shaped 100-nm nanoparticles at each segment of IRONSperm to obtain the ratio of magnetic material per cell segment and its net magnetization (see Materials and Methods and fig. S1). The average magnetic dipole moment of IRONSperm is 5.9×10^{-11} Am^2 at a magnetic field of 5 mT, whereas the average remanent magnetization is 5.2×10^{-11} Am^2. The magnetization vector changes its direction when the field is applied and is enclosed between the local tangent of each segment and the magnetic field at this segment (*45*). The ratio of magnetic material per segment over the total magnetic material per cell for the head, midpiece, principal piece, and distal tip are 31, 8, 51, and 10%, respectively (see Materials and Methods and fig. S1 in supporting information). The samples are likely to have a different distribution of nanoparticles owing to the cell-to-cell variability in surface charge (*38*). These ratios are used in the determination of the magnetic dipole moments of each segment, and Eq. 2 is numerically
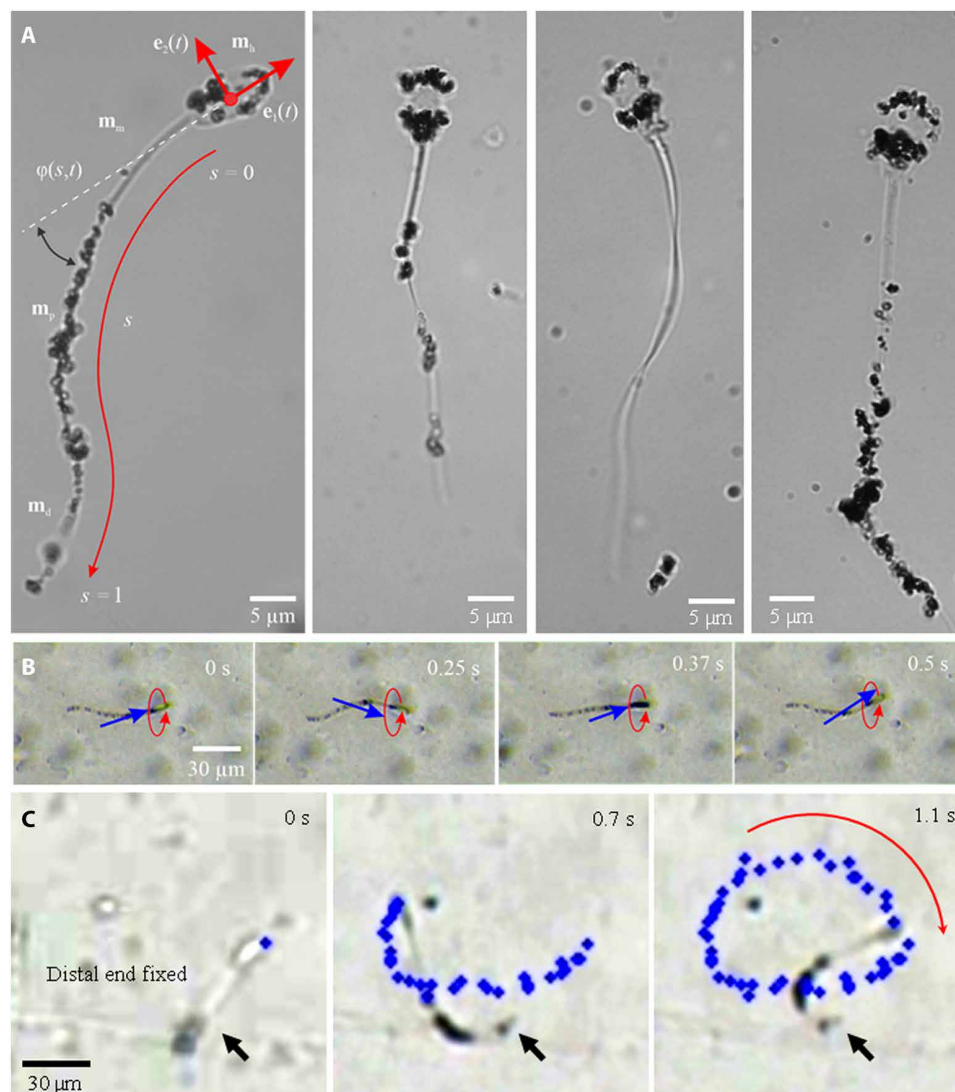
Fig. 2. Bovine sperm cells are coated with rice grain–shaped maghemite nanoparticles resulting in IRONSperms. (**A**) Microscopic images of different cases of IRONSperm indicate the attachment of the nanoparticles to the organic body. $e_1(t)$ and $e_2(t)$ are orthonormal vectors of the material frame of IRONSperm, and the shape of its flagellum is characterized by the tangent angle ($\varphi(s, t)$) as a function of the arc length s. The magnetic moment of the head is oriented along $e_1(t)$ after fabrication. The direction of the magnetic moment is enclosed between the $e_1(t)$ and the magnetic field. Magnetic dipole moment of the head, midpiece, principal piece, and distal end are m_h, m_m, m_p, and m_d, respectively. (**B**) Time-lapse images depicting the flagellar response of IRONSperm to a uniform magnetic field with periodic component at frequency f. The head rotates with constant precession and induces a helical traveling wave along the flagellum and results in forward swimming speed (v). The blue and red arrows indicate the magnetic field and direction of rotation, respectively. See also movie S1. (**C**) The distal end of IRONSperm is fixed, and the head aligns with the magnetic field. The deformation is represented by the blue dots and is approximated by an ellipse with minor and major diameters of 50 and 82 µm, respectively. See movie S2 in supporting information for illustration of the flexible bending.

solved to predict the response of IRONSperm. The contribution of the magnetic torque in Eq. 2 is included by specifying the boundary conditions between each segment (see Materials and Methods). Equation 2 can also be used to predict the response of IRONSperm in close proximity to a solid boundary by specifying the drag coefficient (c_{ni}) as a function of the distance to this boundary (*46*).

Magnetization distribution and magnetic actuation

Similar to sperm cells, IRONSperms display either a planar two-dimensional or a helical three-dimensional flagellar wave (*47*). In the case of a planar flagellar wave, periodic magnetic fields constrained to a plane can be used to propel IRONSperm. In the case of a helical flagellar wave, periodic out-of-plane fields with a cone angle (α_m) enable the head to follow a finite steradian. The axis of the steradian concedes with the long axis of IRONSperm, as shown in Fig. 4A. On the basis of the magnetization distribution experiments and the measured magnetic properties, we enter the measured magnetization of each segment into the hydrodynamic model (Eq. 2). The time-dependent flagellum deformation is calculated for actuation frequency of $1 \leq f \leq 20$ Hz and a magnetic field cone angle of $10° \leq \alpha_m \leq 90°$.

Figure 4A shows the time-dependent flagellum deformation for $f = 1$ Hz and $\alpha = 15°$. The maximum amplitude (vertical distance
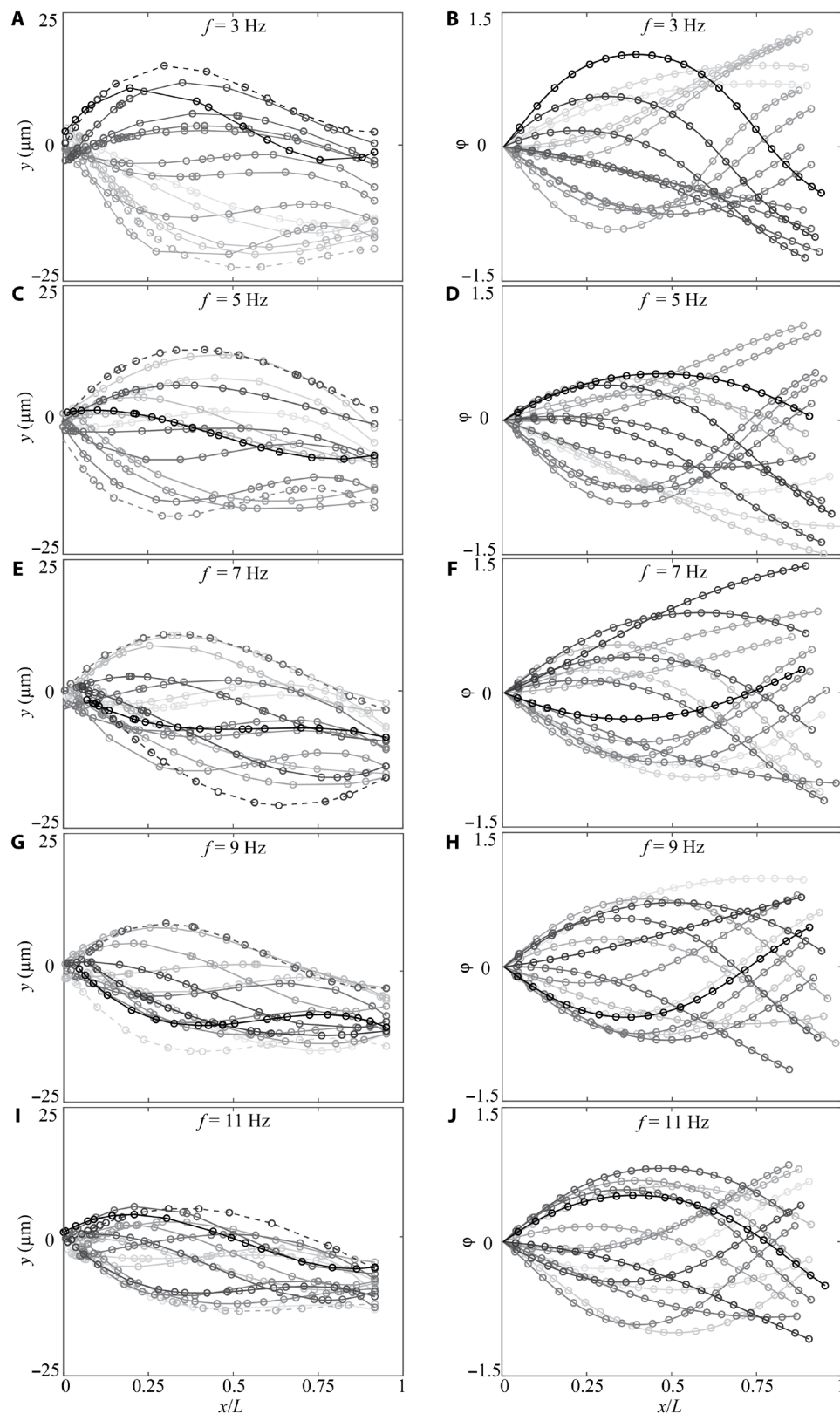
Fig. 3. Time-dependent deformation of the flagellum indicates flexibility of IRONSperm as the actuation frequency (*f*) affects the amplitude of the overall wave pattern. Left column, amplitudes; right column, tangent angles. Darker lines indicate the flagellum at later times, and the dashed lines represent the envelope of the motion. (**A**) Maximum amplitude is 37 μm at *f* = 3 Hz. (**B**) Tangent angle (φ) at 3 Hz. (**C**) Maximum amplitude is 30 μm at *f* = 5 Hz. (**D**) φ at 5 Hz. (**E**) Maximum amplitude is 30 μm at *f* = 7 Hz. (**F**) φ at 7 Hz. (**G**) Maximum amplitude is 23 μm at *f* = 9 Hz. (**H**) φ at 9 Hz. (**I**) Maximum amplitude is 18 μm at *f* = 11 Hz. (D) φ at 11 Hz.

between the propulsion axis e_1 and the envelope) of the propagating wave is 2 μm, producing negligible net thrust. This amplitude is determined on the basis of the transverse deviation from the propulsion axis to the flagellum, as a function of the arc length. For $f = 1$ Hz and α =30°, we also observe a similar response and zero net displacement is achieved for a propagating wave with an amplitude of 4 μm (Fig. 4B). For $f = 1$ Hz and α = 45°, the amplitude of the propagating wave increases to 6 μm (Fig. 4C), producing a net thrust force that propels IRONSperms forward at a speed of 2 μm/s. Therefore, a relatively large cone angle would maximize the amplitude of the propagating wave and enhance the propulsion. The actuation frequency also has a substantial influence on the swimming velocity. Figure 4 (D to F) shows the time-dependent flagellum deformation for actuation frequencies of 1, 5, and 10 Hz and α = 45°, respectively. For $f = 1$ Hz and α = 45°, IRONSperm propels at a speed of 2 μm/s by a propagating wave with an amplitude of 6 μm. For $f = 5$ Hz and α = 45°, the speed increases to 7 μm/s for a wave with an amplitude of 3 μm, as shown in Fig. 4E. For $f = 10$ Hz and α = 45°, a maximum amplitude of 4 μm along the wave is generated and enables IRONSperms to propel at a speed of 9 μm/s (Fig. 4F). The dependence of IRONSperm velocity on cone angle and frequency as calculated by our model is depicted in Fig. 4G. Similar to the cone angle of the actuating magnetic field, the actuation frequency linearly increases the swimming speed and decreases slowly above a step-out frequency of approximately 10 Hz, as shown in Fig. 4G.

Although we have control over the actuation frequency and the cone angle of the magnetic fields, there is intrinsic variation in the distribution of the nanoparticles along the four segments of the sperm cell. The charge distribution of sperm is not uniform and also changes depending on the sperm's developmental state. It is therefore expected that many different configurations of sperm-particle constructs are obtained by self-assembly of nanoparticles with a bull semen sample that naturally contains sperm of different quality. The number of nanoparticles, and also their attachment location on the sperm's membrane, vary from case to case. The large experimental deviation of IRONSperm velocities over the range of applied frequency can thus be explained by the various configurations of IRONsperms.

This variation is evident in the characterized frequency response of IRONSperm, as shown in Fig. 4H. In this experiment, IRONSperms are allowed to swim under the influence of a rotating magnetic field at a frequency range of 0 to 20 Hz. Each data point in Fig. 4H represents the average speed of an IRONSperm sample at the respective actuation frequency. The error bar depicts the SD of the measurements for 15 different samples. At an actuation frequency of 1 Hz, an IRONSperm swims at an average speed of 2.3 ± 1.7 μm/s. The swimming velocity increases linearly with the actuation frequency up to $f = 8$ Hz. At this actuation frequency, the swimming velocity is 6.8 ± 4.1 μm/s, and we observe a step-out behavior above an actuation frequency of 10 Hz. Figure 4 (G and H) shows quantitative
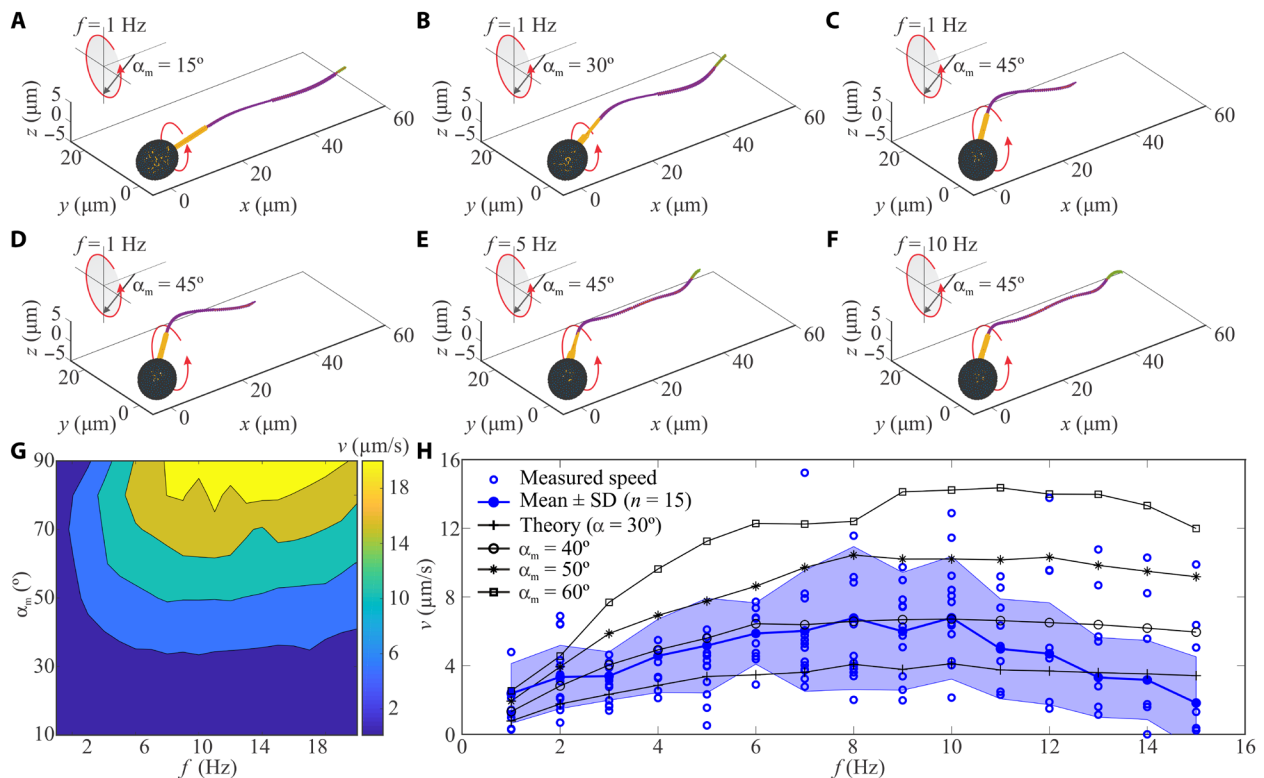

Fig. 4. Swimming speed of IRONSperms is influenced by the actuation frequency (f) and the cone angle of the head (α). The deviations between the magnetization of the segments of the IRONSperm also influence the swimming speed. The flagellum deformation and swimming velocity are calculated for $E = 1$ MPa, $L_m = 13$ μm, $L_p = 40$ μm, $L_d = 7$ μm, $r_m = 0.5$ μm, $r_p = 0.25$ μm, $r_d = 0.25$ μm. $m_h = 4.65 \times 10^{-12}$ Am², $m_m = 1.2 \times 10^{-12}$ Am², $m_p = 7.8 \times 10^{-12}$ Am², $m_d = 1.35 \times 10^{-12}$ Am², $2a = 5$ μm, and $b = 4$ μm. (**A**) $f = 1$ Hz and $α_m = 15°$. (**B**) $f = 1$ Hz and $α_m = 30°$. (**C**) $f = 1$ Hz and $α_m = 45°$. (**D**) $f = 1$ Hz and $α_m = 45°$. (**E**) $f = 5$ Hz and $α_m = 45°$. (**F**) $f = 10$ Hz and $α_m = 45°$. (**G**) Swimming speed (v) is calculated versus the actuation frequency and cone angle. (**H**) Theoretically predicted and experimentally ($n = 15$) obtained swimming speeds of IRONSperm increase linearly with the actuation frequency and decrease slowly above the step-out frequency of 8 Hz.

agreement between our measurements and theoretical predictions. Our theoretical predictions and measurements show that as the angular frequency increases from zero, the swimming velocity increases, reaches a maximum at approximately 8 to 10 Hz, and decreases slowly. In the case that the actuation frequency is below 8 Hz and the cone angle is between 30° to 50°, our measurements are in quantitative agreement with the numerical results. At f = 2 Hz, IRONSperms swim at 3.3 ± 1.8 μm/s, whereas numerical results indicate speeds of 1.7, 2.8, and 3.9 μm/s for cone angles of 30°, 40°, and 50°, respectively. The numerical model predicts also that, as the cone angle increases to 90°, the swimming speed increases. However, this cone angle is not achieved experimentally owing to the limited flexibility of IRONSperm. With a flexible flagellum, the capability of the magnetic head to align with the rotating magnetic field is governed by the magnetoelastic coupling between the flagellum and the magnetic torque. Therefore, the numerical model suggests that, by increasing the cone angle of the head, the swimming velocity increases. In experiments, this enhancement is possible by increasing the applied magnetic field or by increasing the magnetic moment of the head. Increasing the magnetic field is limited by the projection distance from the source, so the magnitude is preferably in the milliTesla range. This range enables the actuating field to span a few centimeters at most, and we limit the magnetic field to 2 mT in all our experiments. In the case of increasing the magnetic moment of the head, the nanoparticle aggregates that coat the sperm cell govern the magneto-elastic coupling. One can increase the induced magnetic torque exerted on the head by increasing the concentration of nanoparticle aggregates per cell. Increasing the concentration generates a stronger torque, but there is an upper limit on the amount of nanoparticles that covers the cell based on the net surface charge between the sperm cell and the particles (Fig. 1F). In addition, our measurements show that the head and principal piece of the cell are, on average, coated with 31 and 51% of the total amount of nanoparticle aggregates, and it is essential to maintain good magnetization and minimal adverse effect on the flexibility of the flagellum.

The flagellar propulsion of IRONSperms and motile sperm cells show good resemblance, although 51% of the nanoparticle aggregates coat its principal piece. A representative flagellar waveform of IRONSperms is illustrated in Fig. 5. In this experiment, a periodic magnetic field is applied at an actuation frequency of 2 Hz using triaxial Helmholtz electromagnetic coils, as shown in Fig. 5A. Figure 5 (B and C) demonstrates the flexibility of the flagellum. First, the time-dependent tail deformation is measured over consecutive beat cycles (Fig. 5B), and the amplitudes of the head and the distal end are measured (Fig. 5C). In contrast to the head, the amplitude of the distal end decreases from 21.2 μm at t = 0 s to 7.9 μm at t = 13 s. We attribute this decrease to the flexibility of the flagellum, which is also influenced by the properties of the medium (consisting of an IRONSperm and nanoparticle aggregates). In this trial, the average swimming speed is measured as 10.8 μm/s. The amplitude of the waveform near the distal end is nearly twice the amplitude near the head, as shown in Fig. 5C. This proves that an asymmetrical shape deformation occurs, which is an important requirement to break Purcell's scallop theorem (48).

Riedel-Kruse et al. (49) and Friedrich et al. (50) have shown that the flagellar shape forms (Figs. 2 and 5D) can be used to determine the zeroth (Ψ_0) and first (Ψ_1) Fourier modes of the Fourier representation of the tangent angle $\varphi(s, t)$. They have implemented this Fourier analysis of the waveforms on two-dimensional projections

of the flagellum during circular swimming near a surface. In our case, the cell is not alive. Its flagellum is passive and does not undergo similar anisotropic and asymmetric beating as live cells (51), which is originated by the active bending moment of the flagellum. Therefore, the flagellar waveform of IRONSperm is preserved during rotation and two-dimensional projections can be used to estimate the time-averaged shape, bending amplitude, and the wave propagation speed. The zeroth mode provides a measure for the asymmetry of the flagella, whereas the first mode is a measure for the magnitude of the bending amplitude along the flagellum and the wavelength. In Fig. 5D, the angle enclosed between the propulsion axis of IRONSperm and the local tangent along the flagellum is calculated from the measured waveform of the flagellum over a complete beat cycle. The zeroth and first Fourier modes are calculated at all arc length positions s, as shown in Fig. 5E. The zeroth mode Ψ_0 indicates that the curvature along the flagellum is approximately 8.8 rad/mm. The curvature is calculated by fitting a line to the zeroth mode data points. Similar to the curvature, the amplitude of the first Fourier mode Ψ_1 indicates that the amplitude rise of the flagellum is 13.5 rad/mm. The amplitude rise is calculated by fitting a line to the amplitude of Ψ_1. Last, the wavelength is calculated by fitting a line to the phase angle of the first Fourier mode of the tangent angle. The calculated wavelength is 150 μm.

Riedel-Kruse et al. (49) and Friedrich et al. (50) have shown that the flagellar waveform of sperm cells is characterized by average curvature, amplitude rise, and wavelength of 13.4 ± 4.8, 14.6 ± 1.2 rad/mm, and 66 ± 8 μm, in water at 36°C. IRONSperms are characterized by a curvature of 8.1 rad/mm, an amplitude rise of 13.5 rad/mm, and a wavelength of 150 μm. Therefore, there is a resemblance between the flagellar waveform of the passive flagellum of IRONSperms and the active flagellum of live sperm cells (52).

Magnetic control and localization

IRONSperms have the capability to swim controllably by a rotating magnetic field produced around an arbitrary axis in space. These fields are generated using a triaxial Helmholtz electromagnetic coil setup, as shown in Fig. 5A. The IRONsperms are actuated in the bulk of the fluid, while unbound nanoparticle aggregates remain at the bottom of the reservoir. A representative open-loop control experiment is demonstrated in Fig. 6A. Rotating magnetic fields are generated around the propulsion axis ($\mathbf{e}_1$) of the flagellum at a frequency of 4 Hz. The propulsion axis ($\mathbf{e}_1$) is oriented toward the bottom-left corner of a square reference trajectory with an edge length of 260 μm. Second, the field is rotated around this axis to generate the flagellar propulsion. At t = 0 s, the IRONSperm is located at the bottom left corner of the square, and its propulsion axis is aligned along the x axis while simultaneously rotating the field. The IRONSperm swims at an average speed of 7.2 μm/s along the square reference trajectory. At t = 47 s, the propulsion axis is rotated along the y axis while simultaneously rotating the field. To keep the IRONSperm in the same plane, the pitch angle of its propulsion axis is set to 15° to compensate for gravitational effects (53). In another open-loop experiment, an IRONSperm is allowed to reverse its swimming direction by rotating the propulsion axis gradually with respect to the z axis, as shown in Fig. 6B. This trial indicates that the IRONSperm undergoes a U-turn trajectory while swimming at an average speed of 12.5 μm/s, under the influence of a rotating magnetic field at 6 Hz. These experiments demonstrate that IRONSperms have the capacity to be actuated using relatively weak magnetic fields (2 mT). The magnetic constituent
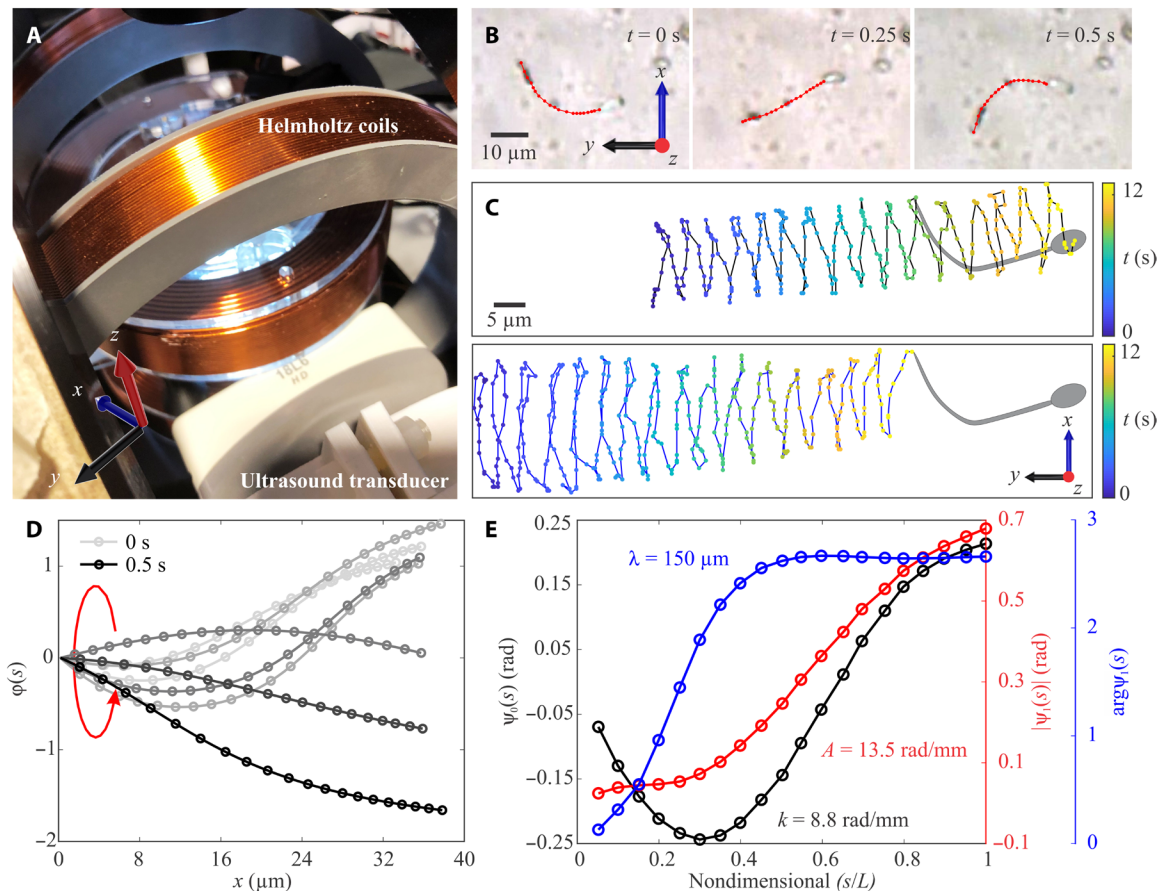
Fig. 5. Flagellar propulsion of IRONSperm is achieved under the influence of rotating magnetic fields. (**A**) Magnetic actuation of IRONSperm is achieved using a triaxial Helmholtz coil electromagnetic system. Photo credit: I.S.M. Khalil. (**B**) IRONSperm is allowed to swim under the influence of a rotating magnetic field at a frequency of 2 Hz. The time-dependent deformation of the flagellum is measured during flagellar propulsion. (**C**) The head aligns along the rotating field with an amplitude of 20 μm. The amplitude of the distal end is 21.2 μm at $t = 0$ s and decreases to 7.9 μm at $t = 13$ s, as indicated by the blue tracking line over a time period of 13 s. The average swimming speed of IRONSperm is 10.8 μm/s. See also movies S3 and S4. (**D**) The tangent angle of the flagellum is calculated from the measured waveform over one beat cycle. (**E**) Curvature ($k = 8.8$ rad/mm), amplitude rise ($A = 13.5$ rad/mm), and wavelength ($\lambda = 150$ μm) are characterized by fitting lines to the zeroth and first Fourier modes of the tangent angle.

of IRONSperm not only offers magnetic remote control and actuation of single sperm cells but also enables localization of groups of IRONSperm using ultrasound images. One of the key challenges of using IRONSperms in targeted in vivo drug delivery applications is the localization and control using a medical imaging modality. Therefore, we investigate the localization of IRONSperms by ultrasound imaging, which is a high-resolution, real-time, and noninvasive medical imaging method (*1*).

The difference in acoustic impedance between sperm cells and their background fluids and soft tissue is relatively low. Therefore, localization of sperm cells using ultrasound feedback is not possible. The magnetic constituent of IRONSperms increases the acoustic impedance and thereby allows the detection of swarms of IRONSperms with ultrasound waves. The diameter and length of the elongated particles that coat IRONSperms are 10 and 100 nm, respectively, while the wavelength of a 10-MHz wave is approximately $1540/(10 \times 10^{-6})$ m = 154 μm. This wavelength dictates the limit of the smallest objects that can be detected. It is possible to coat the whole cell (length of 60 to70 μm) with particles. Even then, only a 20-MHz wave could enable the localization of a single IRONSperm. However,

clusters of IRONSperms can be detected, but a minimum size of the cluster has to be comparable to the wavelength of the wave.

To test the echogenicity of clusters of IRONSperms, we insert samples inside polyethylene tubes with an inner diameter of 380 μm (Fig. 7A). The samples are detected by a 16-MHz wave and visual feedback, as shown in Fig. 7 (B and C), respectively. In this trial, the tube is contained inside a transparent water reservoir to achieve air-free coupling between the tube and the ultrasound transducer. The water reservoir is mounted on an inverted microscope to compare ultrasound scans to microscopic images (Fig. 7A). Figure 7B shows the response of several clusters to an external magnetic field. The length of the clusters is approximately 200 μm and contains several IRONSperm samples. The green arrows indicate the location of these clusters in the ultrasound scans in Fig. 6C. This experiment shows that the magnetic constituent provides a relatively high contrast-to-noise ratio for the detection and localization of IRONSperms.

Loading of a molecular cargo for further therapeutic tasks

Doxorubicin hydrochloride (DOX-HCl), a widely applied anticancer drug, is used as a model drug to evaluate the loading capability of
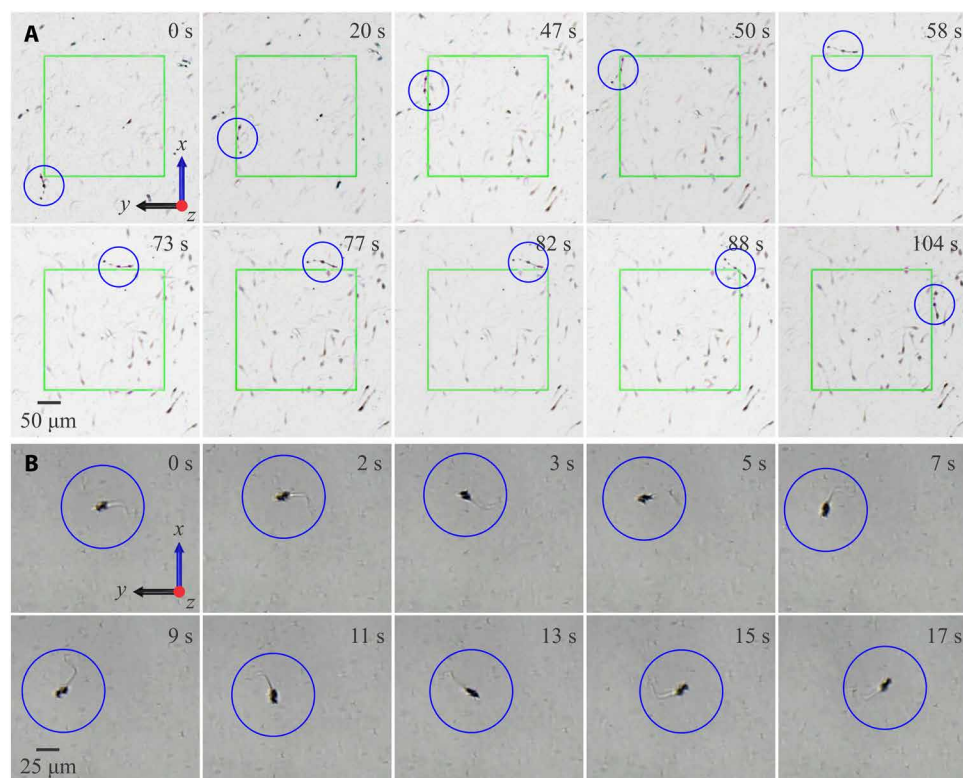
Fig. 6. Control of IRONSperm is achieved using a triaxial Helmholtz coil electromagnetic system. (**A**) IRONSperm samples are contained in the common centers of the coils and controlled by a homogeneous rotating field with a maximum magnitude of 2 mT on a square trajectory. IRONSperm follows a square trajectory with edge length of 260 μm at an average speed of 7.2 μm/s at an actuation frequency of 4 Hz. See also movie S5. (**B**) IRONSperm undergoes a U-turn trajectory at an average speed of 12.5 μm/s at an actuation frequency of 6 Hz. The blue circles indicate IRONSperm. See also movies S5 and S6.

the here-presented IRONSperms (nonviable sperm decorated with magnetic nanoparticles). Thus, both the drug and IRONsperms were coincubated at room temperature and under mild agitation for about 1 hour, adapting an already reported protocol (*29*) (see Materials and Methods). After washing twice with water, drug-loaded IRONsperms were suspended in sperm medium (modified Tyrode's albumin lactate pyruvate medium) to evaluate their drug-loading capability by using fluorescence microscopy and spectrophotometry. As DOX-HCl is autofluorescent at 485-nm excitation wavelength, fluorescent microscopy was sufficient to confirm the presence of the drug in IRONsperms (Fig. 8, A and C). As it can be seen in Fig. 8 (A and B), IRONSperms were successfully loaded with DOX-HCl. In contrast to the previously reported work, where the drug was mainly found in the nucleus of living sperm because of the high affinity of DOX-HCl to DNA (*29*), in the IRONsperms, the drug was found in the whole body, including the midpiece and tail. A possible reason might be the rupture of the sperm membrane during its interaction with the magnetic nanoparticles (in water), which facilitates the drug adsorption on the remaining proteins and lipid layers. However, further investigations using high-resolution microscopy are required to confirm their precise localization. Furthermore, DOX-HCl loading efficiency and loading amount per sperm were determined by optical spectroscopy. After 1 hour of incubation, $11.3 \pm 0.5\%$ of DOX-HCl was taken up by sperms when 1.3×10^6 sperms/ml was immersed in a DOX-HCl solution at a final concentration of 50 μg/ml (see details in the Materials and Methods). A single IRONsperm

was able to load 4.3 ± 0.2 pg of DOX-HCl. This amount was calculated after performing the linear regression of the amount found in the supernatant of the IRONsperm sample (supernatant was diluted 500 times to be in the linear range; see details in the Materials and Methods) (Fig. 8D). The cumulative release test shows the loading stability of the IRONsperm. After 72 hours of incubation, $21.4 \pm 0.5\%$ of the drug was kept inside the IRONsperm (Fig. 8E), although a burst release was observed in the first 8 hours. IRONsperms can be thus envisioned as potential drug carrier, thanks to their high encapsulation capacity and stability.

The biocompatibility of IRONsperm was tested by coculturing IRONsperm with Ishikawa cells, a human endometrial adenocarcinoma cell line. IRONSperms were cocultured with Ishikawa cells for 3 days. After 24 hours and after 3 days, we performed a trypan blue assay, a standard cytotoxicity test that stains any dead cells. No increased number of dead cells was observed after 24 hours or 3 days, respectively, as displayed in fig. S2. This proves the biocompatibility of IRONsperm and thus prospects for biomedical applications.

DISCUSSION
Similar to motile sperm cells, IRONSperms swim by a controlled traveling-wave propagation along their flexible flagella. The incorporation of magnetite nanoparticles onto the cell surface enables the distributed actuation by a rotating magnetic field while maintaining the flexibility of the swimmer. We show that the swimming
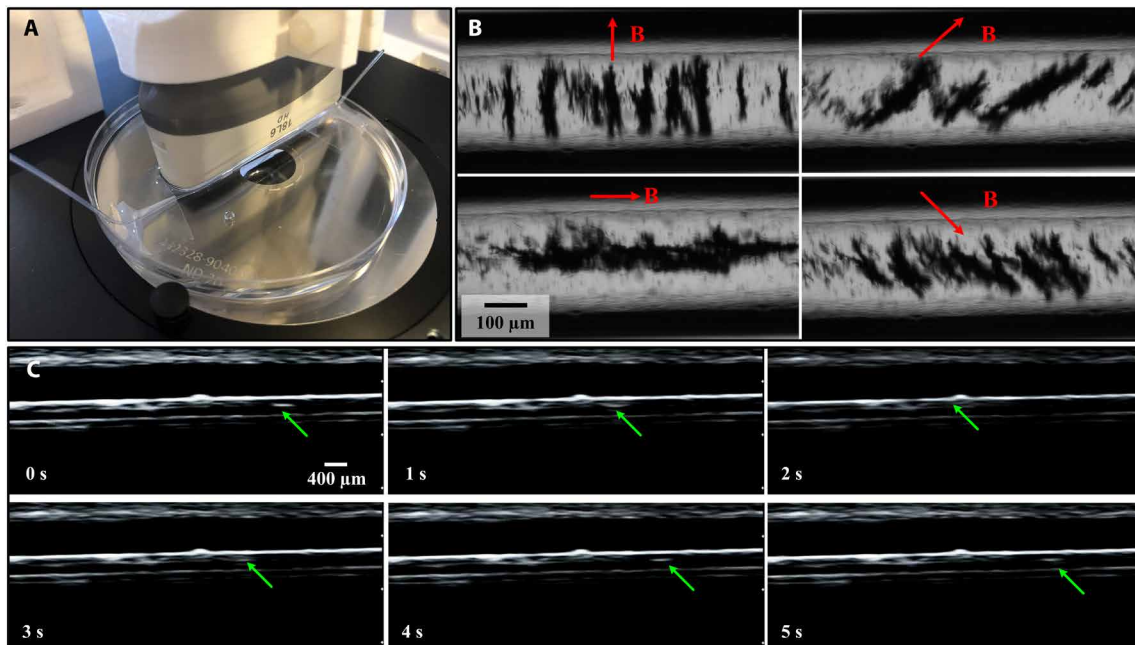
Fig. 7. Ultrasound images showing efficient localization of a cluster of IRONSperm. (**A**) Clusters of IRONSperm samples are contained inside a polyethylene tube with an inner diameter of 380 μm. The tube is submerged inside a water reservoir above an inverted microscope. Photo credit: I.S.M. Khalil. (**B**) Visual feedback is obtained by the microscopic images and indicates several clusters that align with the external magnetic field lines (red arrow). (**C**) Ultrasound scans show a cluster of IRONSperm samples (green arrow) moving with the flowing streams of the medium along one dimension. Parameters: depth = 2 cm, frequency of the ultrasound waves = 16 MHz. See also movie S7.

speed of IRONSperms is influenced by the precession angle of its head and the actuation frequency of the magnetic fields. The theoretical prediction of our numerical model and experimental results suggest an optimal precision/frequency combination. This combination is dependent on the magnetization profile of IRONSperms, which is quantified experimentally to determine the average magnetic dipole moments along the cell. The cell-to-cell variation in the charge distribution influences the magnetization profile. For instance, in the case of localized magnetization only at the head, the waveform of the flagellum is governed by the balance between the hydrodynamic drag and the elastic forces, whereas when the tail is coated with particles that its flexibility is likely to decrease (*52*). Therefore, the flagellar waveform and the corresponding swimming speed are influenced by the magnetization profile. The scatter in the velocity measurements (Fig. 4H) is attributed to the cell-to-cell variability in charge distribution and magnetization profile (*38*). However, the average forward velocity of IRONSperms increases linearly with the frequency until a step-out frequency is reached. It is possible to increase this step-out frequency to keep IRONSperms in sync with the rotating field by increasing the magnetization per cell and the applied field, thus increasing the possibility of actuating all nonmotile sperm cells regardless of their magnetization profile. The nonuniform distribution of the sperm cells opens up additional opportunities to design undulatory systems with selective distributed actuation. Consider, for instance, two microrobots: one with a uniform coating and another with localized magnetization at the head. The expected flagellar waveforms would have a constant curvature and uniform bending amplitude along the flagellum for the microrobot with uniform coating. The curvature of the second microrobot would vary, and the bending amplitude would increase along the flagellum. Therefore, an accurate charge mapping of sperm cells

will enable new microrobot designs with distributed actuation and the desired flagellar waveform.

Our magnetic actuation, drug loading, and localization experiments reveal that IRONSperms provide a unique combination of basic functions, which are fundamental to minimally invasive medicine using microrobotics. The natural design of the sperm cell is preserved to provide essential flexibility for propulsion in a viscosity-dominated flow regime. Only the difference in surface charge is required to achieve successful coupling and magnetization of the cells. Further, our approach allows for the loading of the cells with drugs without affecting the flexibility of the flagellum. Furthermore, the electrostatic-based self-assembly has two fundamentally different contributions. First, it allows us to develop hybrid microbiorobots and actuate nonmotile sperm cells. Second, it changes the acoustic impedance of the sperm cells by the magnetic coating and enables localization using ultrasound images. Overall, this approach presents flexible, biotemplated magnetic microswimmers that hold promise in minimally invasive applications inside the human body. Our study verifies this approach by beginning to address four fundamental hurdles standing between the in vitro trials and translation of microrobots into in vivo experiments. We show the capacity to swim controllably under the influence of a controlled magnetic field (Fig. 6). The nanoparticle coating also makes the samples detectable using a minimally invasive imaging system (Fig. 7). The organic body is loaded with an anticancer drug (Fig. 8). Last, the microrobot consists of biocompatible elements, as demonstrated by cytotoxicity tests (fig. S2).

In future research, the interactions of IRONSperms with the environment and with each other have to be investigated. The adhesion to surroundings has to be avoided: For many microrobots, adhesion to obstacles and surfaces is a major challenge to translate
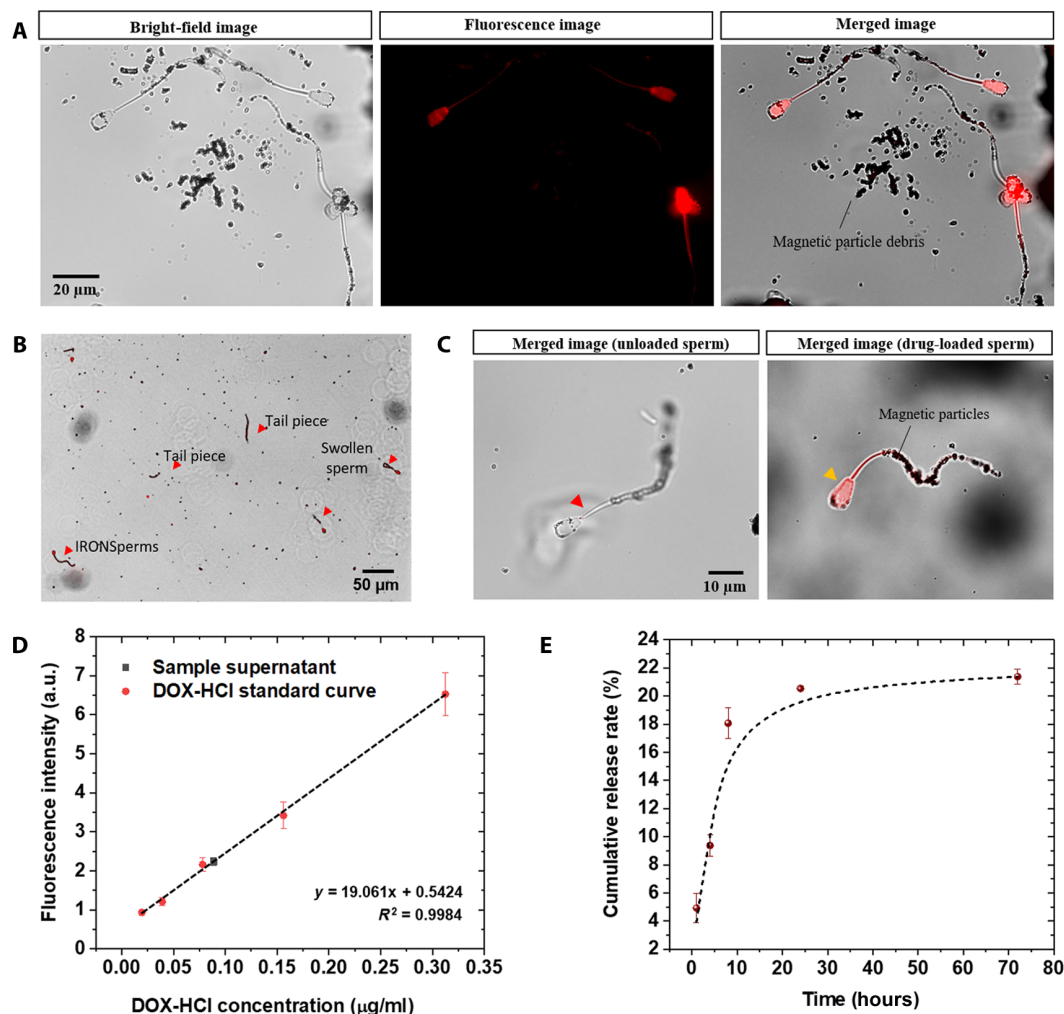
Fig. 8. Drug loading of IRONSperm. (**A**) Fluorescence image of drug-loaded IRONSperms, bright-field overview image of drug-loaded IRONSperms, and merged image. (**B**) Big field view of drug-loaded IRONSperms (×10 magnification, merged image). (**C**) Exemplary image of an unloaded IRONSperm showing no fluorescence and a drug-loaded IRONSperm. (**D**) Spectrophotometry data obtained for different DOX-HCl dilutions (1.25, 0.62, 0.31, 0.16, 0.08, and 0.04 μg/ml), to obtain the corresponding drug concentration present in the IRONSperm sample by linear regression. a.u., arbitrary units. (**E**) Cumulative release rate by IRONSperms over 72 hours. Error bars correspond to four technical replicates.

IRONSperms into conditions encountered in vivo. At the same time, it is expected that soft microrobots provide more gentle interaction with tissue and cells than rigid microrobots, but this remains to be studied in the case of IRONSperms. Targeting cancer cells or other diseases requires detailed analysis of drug release and response of the target tissue. To investigate this application, cell culture, or even better, organ culture, and last, animal studies are required. It is unlikely that a single IRONSperm can deliver a high enough dose of a drug. Therefore, a concerted action of groups of IRONSperms is required. When moving toward in vivo applications, real-time in vivo imaging represents a major challenge. We demonstrate an important step here, which is the imaging of groups of IRONSperms under ultrasound guidance. For the next step, the magnetic guidance of drug-loaded IRONSperms under ultrasound feedback to a target tissue will be achieved. Further, the immune response to our biohybrid microrobots will be tested. All these challenges have to be addressed before the actual translation of IRONSperms into targeted drug delivery applications.

MATERIALS AND METHODS

Synthesis of elongated Fe₂O₃ particles

Rice grain–shaped particles were synthesized following a procedure by Ohmori and Matijević (*54*). A solution of $FeCl_3 \cdot 6H_2O$ (0.02 M) was aged with a NaH_2PO_4 solution (0.0004 M) during 72 hours in a Pyrex bottle at 100°C. The obtained product was centrifuged and washed with acetone. The nanoparticles were repeatedly washed and centrifuged in distilled water.

Fabrication of IRONSperms

Cryo-preserved bovine sperm straws (Masterrind GmbH) were thawed in a 38°C water bath for 2 min and resuspended in sperm medium SP-TALP (Caisson Laboratories, Inc., modified Tyrode's albumin lactate pyruvate medium; one straw per 1 ml of SP-TALP). The sperm suspension was centrifuged for 5 min at 300*g* in a soft mode. The supernatant was discarded, and the pellet was resuspended in distilled water. The sample was centrifuged again with the same settings and lastly resuspended in 500 μl of water.

Particle suspensions were centrifuged and resuspended in distilled water, vortexed, and well suspended by sonicating for 10 min before adding 50 μl of this particle suspension to 50 μl of sperm suspension. The mixture was incubated at room temperature for at least 24 hours before use. Because of the incubation of the bull sperm with particles in deionized water for 24 hours, the spermatozoa were not motile anymore. For storage, the IRONSperm samples were kept at 4°C for several weeks.

Structural characterization and attachment distribution
The average head length of the bovine sperm cells is 8 to 10 μm. The average values for midpiece, principal piece, and distal end are 13, 40, and 7 μm in length, respectively (55–57). The electrostatic self-assembly process causes the nanoparticles to nonuniformly adhere to the four segments of the sperm body. High-resolution microscope images of IRONsperm were obtained with a Leica DMi8 inverted microscope with a 100× oil immersion objective. ImageJ was used to subtract the background and calculate the particle-covered area for each segment (see fig. S1). The ratio between the adhered nanoparticles and each segment is measured. The average surface area of the head, midpiece, principal piece, and distal end are 16.5, 10.7, 56.9, and 11.4 μm^2, respectively. Optical microscopic images (×1000 total magnification, obtained with the Leica DMi8 inverted microscope, 100× oil immersion objective, Leica DFC 450 C camera) of IRONSperms are analyzed, and the ratio of area of adhered nanoparticles of each segment per the total nanoparticle area on the sperm cell is measured as 31, 8, 51, and 10% for the head, midpiece, principal piece, and distal end, respectively.

Cryo–scanning electron microscopy
The cryo-(FE-)SEM SUPRA 40VP-31-79 (Carl Zeiss SMT Ltd., Oberkochen, Germany) equipped with an EMITECH K250X cryo-preparation unit (Quorum Technologies Ltd., Ashford, Kent, UK) was used for imaging of the sperm-particle constructs. Two microliters of suspension was dropped onto a glass slide fixed to the cryo–scanning electron microscope (cryo-SEM) holder and immediately shock-frozen in liquid nitrogen in the slushing chamber. From there, it was transferred to the cryo-preparation chamber at −140°C, sublimed for 15 min at −70°C, and sputter-coated with platinum (layer thickness ca. 6 nm). Subsequently, it was transferred to the SEM and then examined in a frozen state at 5-kV accelerating voltage and −100°C temperature using the secondary electron detector.

Fluidic and structural effects
IRONSperm consists of a bovine sperm cell with nonuniform iron oxide nanoparticle coating. The prolate spheroidal head of length $2a$ and radius b has an average magnetic moment $\mathbf{m}_h$. The head is connected to a midpiece of length l_m and radius r_m and average magnetic moment $\mathbf{m}_m$. Flagellar beat is achieved by the principal piece and the distal end of the flagellum (radius r_f and r_d) with length of l_p and l_d and magnetic moment of $\mathbf{m}_p$ and $\mathbf{m}_d$, respectively. Flagellar wave propagation along the flagellum (with bending stiffness κ) is achieved by exerting a dynamic magnetic torque on the magnetic moments of IRONSperm. This wave propagation enables IRONSperm to swim in a medium with viscosity μ, characterized by low–Reynolds number hydrodynamics (Re = $\rho v_x(L + 2a)/\mu$) where ρ, μ, and L are the density and viscosity of the medium and the length of the flagellum, respectively. Further, v_x is the swimming speed of IRONSperm. At actuation frequency range of 1 to 20 Hz,

the average swimming speed varies between 0.007 to 0.5 body length/s, and Re is on the order of $\mathcal{O}(10^{-4})$. In this regime, the deformation of the flagellum is governed by elastic forces and viscous forces as follows

$$\kappa_i \frac{\partial^4 \varphi_i}{\partial s^4}(s_i, t) + c_{n_i}\frac{\partial \varphi_i}{\partial t}(s, t) = 0 \text{ for } i = \text{h, m, p, d} \quad (3)$$

where κ_i is the bending stiffness of the ith segment along IRONSperm and $\varphi_i(s, t)$ is its tangent angle. Further, c_{n_i} is the normal drag coefficient of the ith segment and given by

$$c_{n_i} = 4\pi\mu / \left(\ln\left(\frac{l_i}{r_i}\right) + 0.193 \right) \quad (4)$$

The influence of a nearby surface can be incorporated into the normal drag coefficient to study the response of IRONSperm near a surface (46). In (Eq. 3), $\varphi_i(s, t)$ represents the deformation of the ith segment of IRONSperm, relative to a fixed frame of reference $(\mathbf{e}_1(t), \mathbf{e}_2(t))$, where $\mathbf{e}_1(t)$ and $\mathbf{e}_2(t)$ are orthonormal vectors such that $\mathbf{e}_1(t)$ is oriented along the long axis of the head. The position coordinates are calculated using

$$x_i(s, t) = x_i(0, t) + \sum_{s=0}^{s}\Delta s \cos(\varphi_i(s, t))$$
$$y_i(s, t) = y_i(0, t) + \sum_{s=0}^{s}\Delta s \sin(\varphi_i(s, t)) \quad (5)$$
$$z_i(s, t) = y_i(s, t - T/4)$$

The period time T is related to angular frequency by $T = 2\pi/\omega$ (Eq. 2), and Δs is the discretization length $\Delta s = \frac{(l_m + l_p + l_d)}{N}$ with $N = 100$. The contribution of the magnetic torque ($\mathbf{m}_i \times \mathbf{B}$) is included by specifying the boundary conditions between each segment, where $\mathbf{B}$ is the external magnetic field with the following components

$$\mathbf{B} = B\begin{pmatrix} \cos(\alpha_h) \\ \sin(\alpha_h)\cos(\omega t) \\ \sin(\alpha_h)\sin(\omega t) \end{pmatrix} \quad (6)$$

The head follows the magnetic field. At the right boundary of the head and the left boundary of the midpiece, $s = 0$, the midpiece orientation is $\varphi_m(0, t) = \alpha_m \sin(\omega t)$. At the right boundary of the midpiece, $s = l_m$, and the left boundary of the principal piece, $s = l_m$, the boundary condition is $\varphi_m(l_m, t) = \varphi_p(l_m, t) = \alpha_p \sin(\omega t)$. At the right boundary of the principal piece, $s = l_m + l_p$, and the left boundary of the distal end, the orientation is $\varphi_p(l_p + l_m, t) = \varphi_d(l_m + l_p, t) = \alpha_d \sin(\omega t)$. At the right boundary of the distal end, $s = L$, the flagellum is free from external forces and torques. Therefore, $\frac{\partial^2 \varphi_d(L, t)}{\partial s^2} = 0$ and $\frac{\partial^3 \varphi_d(L, t)}{\partial s^3} = 0$. The magnetic variables α_m, α_p, and α_d are determined by minimizing the magnetic energy $U = -\sum_i \mathbf{m}_i \cdot \mathbf{B} + 0.5\int_{s=0}^{s=L}\kappa_i\left(\frac{d\varphi_i}{ds}\right)^2 ds$, for $i = $ h, m, p, d. The magnetization vectors are given by

$$\mathbf{m}_i = m_i\begin{pmatrix} (x_i(s + \Delta s, t) - x_i(s, t)) \\ (y_i(s + \Delta s, t) - y_i(s, t)) \\ (z_i(s + \Delta s, t) - z_i(s, t)) \end{pmatrix} / \left| \begin{pmatrix} (x_i(s + \Delta s, t) - x_i(s, t)) \\ (y_i(s + \Delta s, t) - y_i(s, t)) \\ (z_i(s + \Delta s, t) - z_i(s, t)) \end{pmatrix} \right| \quad (7)$$

The angle of the magnetization of each segment is enclosed between the local tangent and the magnetic field for each segment along IRONSperm (45). Stokeslet points are distributed randomly on the surface of an ellipsoid representing the head with distance Δs between the points (58, 59). Along the tail (x_i, y_i, and z_i), Stokeslet points are created in circles of radius r_i perpendicular to the tail tangent. The average distance between Stokeslet points is Δs. The speed of the Stokeslet points (x_N, y_N, and z_N), is defined as $\mathbf{u}_N = (V_x, -\omega z_i, \omega y_i)$. With the Stokeslet relation relating force $\mathbf{F} = [F_1, \ldots F_N]$ with velocities via the matrix $\mathbf{A}$ (60). The total force the propulsion axis (x axis) is determined for each V_x till the force in x direction is zero. This force balance provides the force free speed V_x.

Magnetic characterization and magnetic actuation

The magnetic moment of IRONSperm samples was measured using a vibrating sample magnetometer (VSM), Oxford Instruments, equipped with a variable temperature insert. For this purpose, the IRONSperm suspension in distilled water containing a concentration of 1.7×10^5 cells/ml was placed in a plastic container and then attached to a sample holder made of polyether ether ketone material. The subsequent measurements were carried out at a temperature $T = 300$ K, a measurement frequency $f = 55$ Hz, and an amplitude $x = 1$ mm after calibration (determination of the geometry factor) with a nickel sample. The results show a hysteresis in the range of the external magnetic field $\mu_0 H = \pm 2$ T, characteristic for ferro- and ferrimagnetic materials. The curve and the low coercive field strength $\mu_0 H < 0.1$ T show the soft magnetic character of the magnetic sample fraction. The remanent magnetic moment of $m_r = 5.2 \times 10^{-11}$ Am^2 is considerably smaller than the specific value of the magnetic starting material. Because of the known cell concentration in the suspension, the measured magnetic moment was related to the amount of IRONSperms in the sample. Samples with concentration of 1.7×10^5 cells/ml provide a maximum magnetic dipole moment of 4×10^{-10} Am^2 at magnetic field of 2 T for each IRONSperm.

Frequency response experiments were performed at a maximum magnetic field of 5 mT, and the average magnetic dipole moment of IRONSperms is 5.9×10^{-11} Am^2 (at 5mT). The propulsion of IRONSperms is conducted on a triaxial Helmholtz coil system. The samples are contained in the common center of three orthogonal nested solenoids. The outer diameter of the outer, middle, and inner solenoids is 16, 12, and 7 cm, respectively. The system generates a maximum magnetic field of 5 mT using a current input of 1 A. The samples are actuated by homogeneous magnetic fields with a periodically varying component to enable the head to follow a finite steradian and induce a helical traveling wave along the flagellum.

Drug loading into IRONsperms

Bovine sperm cells with the immobilized magnetic nanoparticles at a concentration of 1.3×10^6 sperms/ml were suspended in a final concentration of DOX-HCl of 50 µg/ml and coincubated at room temperature for ca. 1 hour. After the sample was washed twice with water by centrifugation at 300g for 5 min, the pellet of drug-loaded IRONSperm was redispersed in SP-TALP [modified Tyrode's albumin lactate pyruvate medium (Caisson Laboratories, Inc.)] and stored under dark conditions before fluorescence imaging analysis. Fluorescence images were taken at an excitation wavelength of 470 nm (DOX-HCl: excitation, 470 nm; emission, 580 nm; Cell Observer, Carl Zeiss Microscopy GmbH).

To determine the drug loading efficiency, samples of DOX-HCl solution were prepared in a series of concentrations (1.25, 0.62, 0.31, 0.16, 0.08, and 0.04 µg/ml) to obtain the calibration curve in the linear range. After incubation of sperms in drug solution (50 µg/ml), the respective supernatant was collected after centrifugation and filtered through a 2-µm–pore size membrane. The concentration of DOX-HCl was determined with a fluorescence spectrometer in a fluorescence intensity mode (SpectraMax M2, Molecular Devices LLC), and the total concentration was calculated considering that the sample supernatant had to be diluted 500 times to be in the linear range of the drug calibration curve (Fig. 7D). After doing the linear regression and by multiplying the resulting value 500 times, the total amount of drug found in the supernatant was about 44.4 µg/ml. If the initial drug concentration was 50 µg/ml, the expected amount of drug loaded on the IRONsperm and surrounding particles is then the difference between the initial drug concentration and the measured drug concentration in the supernatant resulting in ca. 5.7 µg/ml DOX-HCl. Then, by dividing 5.67 µg/ml by 1.3×10^6 sperms/ml, an amount of 4.26 ± 0.2 pg per sperm was obtained.

The accumulative release test was performed as reported elsewhere (29). DOX-HCl–loaded IRONsperms were incubated under dark conditions. At each time point (Fig. 7E), the samples were centrifuged, and 0.2 ml of supernatant was collected and replaced with 0.2 ml of water. The accumulative release ration was calculated as the ratio of the accumulated amount of released drug to the total loaded drug. SDs correspond to four technical replicates.

Cytotoxicity tests

Ishikawa cells were cultured in Dulbecco's modified Eagle's medium/F12 medium containing 10% fetal calf serum, 1% insulin, and 1% penicillin/streptomycin at 37°C and 5% CO_2. IRONsperms were prepared as described above from two cryo-preserved semen straws by incubating the thawed and washed sperm with iron oxide particles, resulting in 10^7 IRONsperms. These IRONsperms were centrifuged and resuspended in 300 µl of phosphate-buffered saline (PBS) and distributed equally on three cell flasks, each containing 5 ml of Ishikawa cells in culture. After 24 hours of coculture at 37°C, the culture medium was removed, and 100 µl of PBS was added directly to the culture flasks. Then, 100 µl of 0.4% sterile-filtered Trypan Blue solution (Sigma-Aldrich) was added to each cell flask to obtain 0.2% trypan blue solution. The cells in each flask were immediately imaged with a Leica DMi8 inverted microscope.

REFERENCES AND NOTES

1. B. J. Nelson, I. K. Kaliakatsos, J. J. Abbott, Microrobots for minimally invasive medicine. *Annu. Rev. Biomed. Eng.* **12**, 55–85 (2010).
2. M. Sitti, H. Ceylan, W. Hu, J. Giltinan, M. Turan, S. Yim, E. Diller, Biomedical applications of untethered mobile milli/microrobots. *Proc. IEEE Inst. Electr. Electron. Eng.* **103**, 205–224 (2015).
3. J. Li, B. Esteban-Fernández de Ávila, W. Gao, L. Zhang, J. Wang, Micro/nanorobots for biomedicine: Delivery, surgery, sensing, and detoxification. *Sci. Robot.* **2**, eaam6431 (2017).
4. L. Zhang, T. Petit, Y. Lu, B. E. Kratochvil, K. E. Peyer, R. Pei, J. Lou, B. J. Nelson, Controlled propulsion and cargo transport of rotating nickel nanowires near a patterned solid surface. *ACS Nano* **4**, 6228–6234 (2010).
5. M. P. Kummer, J. J. Abbott, B. E. Kratochvil, R. Borer, A. Sengul, B. J. Nelson, OctoMag: An electromagnetic system for 5-DOF wireless micromanipulation. *IEEE Trans. Robot.* **26**, 1006–1017 (2010).

6. M. Medina-Sánchez, L. Schwarz, A. K. Meyer, F. Hebenstreit, O. G. Schmidt, Cellular cargo delivery: Toward assisted fertilization by sperm-carrying micromotors. *Nano Lett.* **16**, 555–561 (2015).

7. H. Xie, M. Sun, X. Fan, Z. Lin, W. Chen, L. Wang, L. Dong, Q. He, Reconfigurable magnetic microrobot swarm: Multimode transformation, locomotion, and manipulation. *Sci. Robot.* **4**, eaav8006 (2019).

8. W. F. Paxton, K. C. Kistler, C. C. Olmeda, A. Sen, S. K. St. Angelo, Y. Cao, T. E. Mallouk, P. E. Lammert, V. H. Crespi, Catalytic nanomotors: Autonomous movement of striped nanorods. *J. Am. Chem. Soc.* **126**, 13424–13431 (2004).

9. W. Wang, L. A. Castro, M. Hoyos, T. E. Mallouk, Autonomous motion of metallic microrods propelled by ultrasound. *ACS Nano* **6**, 6122–6132 (2012).

10. J. Li, T. Li, T. Xu, M. Kiristi, W. Liu, Z. Wu, J. Wang, Magneto-acoustic hybrid nanomotor. *Nano Lett.* **15**, 4814–4821 (2015).

11. P. Calvo-Marzal, S. Sattayasamitsathit, S. Balasubramanian, J. R. Windmiller, C. Dao, J. Wang, Propulsion of nanowire diodes. *Chem. Commun.* **46**, 1623–1624 (2010).

12. S. Palagi, A. G. Mark, S. Y. Reigh, K. Melde, T. Qiu, H. Zeng, C. Parmeggiani, D. Martella, A. Sanchez-Castillo, N. Kapernaum, F. Giesselmann, D. S. Wiersma, E. Lauga, P. Fischer, Structured light enables biomimetic swimming and versatile locomotion of photoresponsive soft microrobots. *Nat. Mater.* **15**, 647–653 (2016).

13. A. Servant, F. Qiu, M. Mazza, K. Kostarelos, B. J. Nelson, Controlled in vivo swimming of a swarm of bacteria-like microrobotic flagella. *Adv. Mater.* **27**, 2981–2988 (2015).

14. X. Yan, Q. Zhou, M. Vincent, Y. Deng, J. Yu, J. Xu, T. Xu, T. Tang, L. Bian, Y.-X. J. Wang, K. Kostarelos, L. Zhang, Multifunctional biohybrid magnetite microrobots for imaging-guided therapy. *Sci. Robot.* **2**, eaaq1155 (2017).

15. A. Aziz, M. Medina-Sánchez, J. Claussen, O. G. Schmidt, Real-time optoacoustic tracking of single moving micro-objects in deep phantom and ex vivo tissues. *Nano Lett.* **19**, 6612–6620 (2019).

16. J. Li, X. Li, T. Luo, R. Wang, C. Liu, S. Chen, D. Li, J. Yue, S.-h. Cheng, D. Sun, Development of a magnetic microrobot for carrying and delivering targeted cells. *Sci. Robot.* **3**, eaat8829 (2018).

17. J. Park, C. Jin, S. Lee, J.-Y. Kim, H. Choi, Magnetically actuated degradable microrobots for actively controlled drug release and hyperthermia therapy. *Adv. Healthc. Mater.* **8**, 1900213 (2019).

18. L. Ricotti, B. Trimmer, A. W. Feinberg, R. Raman, K. K. Parker, R. Bashir, M. Sitti, S. Martel, P. Dario, A. Menciassi, Biohybrid actuators for robotics: A review of devices actuated by living cells. *Sci. Robot.* **2**, eaaq0495 (2017).

19. B. J. Williams, S. V. Anand, J. Rajagopalan, M. T. A. Saif, A self-propelled biohybrid swimmer at low Reynolds number. *Nat. Commun.* **5**, 3081 (2014).

20. V. Magdanz, S. Sanchez, O. G. Schmidt, Development of a sperm-flagella driven micro-bio-robot. *Adv. Mater.* **25**, 6581–6588 (2013).

21. B. Behkam, M. Sitti, Bacterial flagella-based propulsion and on/off motion control of microscale objects. *Appl. Phys. Lett.* **90**, 023902 (2007).

22. M. M. Stanton, J. Simmchen, X. Ma, A. Miguel-López, S. Sánchez, Biohybrid Janus motors driven by *Escherichia coli. Adv. Mater. Interfaces* **3**, 1500505 (2016).

23. V. Magdanz, M. Medina-Sánchez, L. Schwarz, H. Xu, J. Elgeti, O. G. Schmidt, Spermatozoa as functional components of robotic microswimmers. *Adv. Mater.* **29**, 1606301 (2017).

24. Y. Alapan, O. Yasa, B. Yigit, I. C. Yasa, P. Erkoc, M. Sitti, Microrobotics and microorganisms: Biohybrid autonomous cellular robots. *Annu. Rev. Control. Robot. Auton. Syst.* **2**, 205–230 (2019).

25. O. Yasa, P. Erkoc, Y. Alapan, M. Sitti, Microalga-powered microswimmers toward active cargo delivery. *Adv. Mater.* **30**, e1804130 (2018).

26. J. Zhuang, R. W. Carlsen, M. Sitti, pH-taxis of biohybrid microsystems. *Sci. Rep.* **5**, 11403 (2015).

27. A. Sahari, M. A. Traore, B. E. Scharf, B. Behkam, Directed transport of bacteria-based drug delivery vehicles: Bacterial chemotaxis dominates particle shape. *Biomed. Microdevices* **16**, 717–725 (2014).

28. O. Felfoul, M. Mohammadi, S. Taherkhani, D. de Lanauze, Y. Zhong Xu, D. Loghin, S. Essa, S. Jancik, D. Houle, M. Lafleur, L. Gaboury, M. Tabrizian, N. Kaou, M. Atkin, T. Vuong, G. Batist, N. Beauchemin, D. Radzioch, S. Martel, Magneto-aerotactic bacteria deliver drug-containing nanoliposomes to tumour hypoxic regions. *Nat. Nanotechnol.* **11**, 941–947 (2016).

29. H. Xu, M. Medina-Sánchez, V. Magdanz, L. Schwarz, F. Hebenstreit, O. G. Schmidt, Sperm-hybrid micromotor for targeted drug delivery. *ACS Nano* **12**, 327–337 (2018).

30. W. Gao, X. Feng, A. Pei, C. R. Kane, R. Tam, C. Hennessy, J. Wang, Bioinspired helical microswimmers based on vascular plants. *Nano Lett.* **14**, 305–310 (2014).

31. K. Kamata, Z. Piao, S. Suzuki, T. Fujimori, W. Tajiri, K. Nagai, T. Iyoda, A. Yamada, T. Hayakawa, M. Ishiwara, S. Horaguchi, A. Belay, T. Tanaka, K. Takano, M. Hangyo, *Spirulina*-templated metal microcoils with controlled helical structures for THz electromagnetic responses. *Sci. Rep.* **4**, 4919 (2015).

32. S. K. Srivastava, M. Medina-Sánchez, B. Koch, O. G. Schmidt, Medibots: Dual-action biogenic microdaggers for single-cell surgery and drug release. *Adv. Mater.* **28**, 832–837 (2015).

33. M. Sun, X. Fan, X. Meng, J. Song, W. Chen, L. Sun, H. Xie, Magnetic biohybrid micromotors with high maneuverability for efficient drug loading and targeted drug delivery. *Nanoscale* **11**, 18382–18392 (2019).

34. H.-W. Huang, F. E. Uslu, P. Katsamba, E. Lauga, M. S. Sakar, B. J. Nelson, Adaptive locomotion of artificial microswimmers. *Sci. Adv.* **5**, eaau1532 (2019).

35. M. Medina-Sánchez, V. Magdanz, M. Guix, V. M. Fomin, O. G. Schmidt, Swimming microrobots: Soft, reconfigurable, and smart. *Adv. Funct. Mater.* **28**, 1707228 (2018).

36. I. S. M. Khalil, A. Fatih Tabak, A. Klingner, M. Sitti, Magnetic propulsion of robotic sperms at low-Reynolds number. *Appl. Phys. Lett.* **109**, 033701 (2016).

37. V. Magdanz, J. Gebauer, D. Mahdi, J. Simmchen, I. S. M. Khalil, in *International Conference on Manipulation, Automation and Robotics at Small Scales (MARSS)*, (IEEE, 2019), pp. 1–6.

38. V. Magdanz, J. Gebauer, P. Sharan, S. Eltoukhy, D. Voigt, J. Simmchen, Sperm–particle interactions and their prospects for charge mapping. *Adv. Biosyst.* **3**, 1900061 (2019).

39. A. Kirillova, G. Stoychev, A. Synytska, Programmed assembly of oppositely charged homogeneously decorated and Janus particles. *Faraday Discuss.* **191**, 89–104 (2016).

40. D. Ortiz, K. L. Kohlstedt, T. D. Nguyen, S. C. Glotzer, Self-assembly of reconfigurable colloidal molecules. *Soft Matter* **10**, 3541–3552 (2014).

41. D. J. Griffiths, *Introduction to Electrodynamics*, 4th edition (Pearson, 2013), pp. 312–321.

42. C. H. Wiggins, R. E. Goldstein, Flexive and propulsive dynamics of elastica at low Reynolds number. *Phys. Rev. Lett.* **80**, 3879–3882 (1998).

43. T. S. Yu, E. Lauga, A. E. Hosoi, Experimental investigations of elastic tail propulsion at low Reynolds number. *Phys. Fluids* **18**, 091701 (2006).

44. K. E. Machin, Wave propagation along Flagella. *J. Exp. Biol.* **35**, 796–806 (1958).

45. J. J. Abbott, O. Ergeneman, M. P. Kummer, A. M. Hirt, B. J. Nelson, Modeling magnetic torque and force for controlled manipulation of soft-magnetic bodies. *IEEE Trans. Robot.* **23**, 1247–1252 (2007).

46. C. Brennen, H. Winet, Fluid mechanics of propulsion by cilia and flagella. *Annu. Rev. Fluid Mech.* **9**, 339–398 (1977).

47. D. M. Woolley, G. G. Vernon, A study of helical and planar waves on sea urchin sperm flagella, with a theory of how they are generated. *J. Exp. Biol.* **204**, 1333–1345 (2001).

48. E. M. Purcell, Life at low Reynolds number. *Am. J. Phys.* **45**, 3–11 (1977).

49. I. H. Riedel-Kruse, A. Hilfinger, J. Howard, F. Jülicher, How molecular motors shape the flagellar beat. *HFSP J.* **1**, 192–208 (2007).

50. B. M. Friedrich, I. H. Riedel-Kruse, J. Howard, F. Jülicher, High-precision tracking of sperm swimming fine structure provides strong test of resistive force theory. *J. Exp. Biol.* **213**, 1226–1234 (2010).

51. H. Gadêlha, P. Hernández-Herrera, F. Montoya, A. Darszon, G. Corkidi, The human sperm beats anisotropically and asymmetrically in 3D. *bioRxiv*, 795245 (2019).

52. I. S. M. Khalil, V. Magdanz, J. Simmchen, A. Klingner, S. Misra, Resemblance between motile and magnetically actuated sperm cells. *Appl. Phys. Lett.* **116**, 063702 (2020).

53. A. W. Mahoney, J. C. Sarrazin, E. Bamberg, J. J. Abbott, Velocity control with gravity compensation for magnetic helical microswimmers. *Adv. Robot.* **25**, 1007–1028 (2011).

54. M. Ohmori, E. Matijević, Preparation and properties of uniform coated colloidal particles. VII. Silica on hematite. *J. Colloid Interface Sci.* **150**, 594–598 (1992).

55. J. M. Cummins, P. F. Woodall, On mammalian sperm dimensions. *J. Reprod. Fertil.* **75**, 153–175 (1985).

56. S. K. Shahani, S. G. Revell, C. G. Argo, R. D. Murray, Mid-piece length of spermatozoa in different cattle breeds and its relationship to fertility. *Pak. J. Biol. Sci.* **13**, 802–808 (2010).

57. V. Magdanz, S. Boryshpolets, C. Ridzewski, B. Eckel, K. Reinhardt, The motility-based swim-up technique separates bull sperm based on differences in metabolic rates and tail length. *PLOS ONE* **14**, e0223576 (2019).

58. R. Cortez, The method of regularized Stokeslets. *SIAM J. Sci. Comput.* **23**, 1204–1225 (2001).

59. R. Cortez, L. Fauci, A. Medovikov, The method of regularized Stokeslets in three dimensions: Analysis, validation, and application to helical swimming. *Phys. Fluids* **17**, 031504 (2005).

60. D. J. Smith, A nearest-neighbour discretisation of the regularized stokeslet boundary integral equation. *J. Comput. Phys.* **358**, 88–102 (2018).

Citation: V. Magdanz, I. S. M. Khalil, J. Simmchen, G. P. Furtado, S. Mohanty, J. Gebauer, H. Xu, A. Klingner, A. Aziz, M. Medina-Sánchez, O. G. Schmidt, S. Misra, IRONSperm: Sperm-templated soft magnetic microrobots. *Sci. Adv.* **6**, eaba5855 (2020).